Real-time measurement of minimum cross-sectional area and radius of curvature of miniature plate specimens using a high-speed laser profiler for calculating true stress-true strain curves

OPEN ACCESS
IOP Publishing
Measurement Science and Technology
Meas. Sci. Technol. **34** (2023) 075015 (11pp)
https://doi.org/10.1088/1361-6501/acca38

Real-time measurement of minimum cross-sectional area and radius of curvature of miniature plate specimens using a high-speed laser profiler for calculating true stress-true strain curves

Taichiro Kato*, **Xiaoyong Ruan and Takashi Nozawa**

National Institutes for Quantum Science and Technology, 2-166 Oaza-Obuchi-Aza-Omotedate, Rokkasho-mura, Kamikita-gun, Aomori 039-3212, Japan

E-mail: kato.taichiro@qst.go.jp

Received 12 January 2023, revised 15 March 2023
Accepted for publication 4 April 2023
Published 20 April 2023

Abstract

True stress-true strain curves are fundamental for designing and analyzing structures such as fusion reactors. These curves are typically obtained by conducting tensile tests on round bar specimens. However, due to material dimension limitations, plate specimens are sometimes used instead of round bar specimens. Obtaining true stress-true strain curves experimentally from plate specimens can be challenging. To address this challenge, this study aims to obtain true stress-true strain curves of miniature plate specimens using both analytical and experimental methods. The analytical method involved inverse finite element method (FEM), while the experimental method utilized real-time measurement of the minimum cross-sectional area and radius of curvature of a miniature plate specimen with a high-speed laser profiler. Comparing the true stresses obtained from the analytical and experimental methods, we found that the difference was typically within 5%. These findings suggest that inverse FEM and laser profilometry are effective methods for determining the true stress-true strain of miniature plate specimens.

Keywords: true stress-true strain curve, miniature plate specimen, minimum cross-sectional area, radius of curvature, high-speed laser profiler, real-time measurement

(Some figures may appear in colour only in the online journal)

* Author to whom any correspondence should be addressed.

1. Introduction

Power generation through fusion reactions is expected to be a significant energy source in the future [1, 2]. In fusion reactors, blanket modules are essential components that are subjected to neutron irradiation during the fusion reaction. This irradiation can cause material hardening due to irradiation effects [3]. For example, in reduced activation ferritic steel F82H, one of the candidates structural materials for fusion reactors, neutron irradiation can displace interstitial atoms and generate various lattice defect aggregates by displaced atoms and vacancies. This results in shape changes due to the so-called void swelling [4–6]. Irradiation effects on material properties have been found to increase tensile strength and decrease elongation compared to unirradiated materials [7–10]. It is challenging to design fusion reactors within elastic deformation due to reduced elastic deformation capacity caused by irradiation effects, and thus design within the elastic-plastic range is being considered [11, 12]. True stress (equivalent stress) and true strain (equivalent strain), which are crucial material parameters for the design and analysis of fusion reactors and other structures, are typically obtained through tensile testing using round bar specimens [13–15]. Recently, a method to obtain true stress and true strain from nominal stress and nominal strain by inverse finite element method (iFEM) analysis has been developed. It has been reported that this method shows good agreement with the true stress and true strain obtained by experimental methods [16–18].

It is well-known that to calculate true stress and true strain after the onset of necking from experimental data, tensile tests are conducted on round bar specimens, and the results are applied to Bridgman's equation [15]. To apply Bridgman's equation to plate specimens, average stress obtained by dividing the incremental test load by the incremental minimum cross-sectional area, the radius of curvature at the neck, and the specimen half-width are required to calculate true stress. Among these parameters, measurement of the minimum cross-sectional area has been a challenge. Previous papers on the measurement of the minimum cross-sectional area have been unclear about the measurement method or have had problems with measurement accuracy [9, 19–22]. Recently, our group has used image measurement using reflected and transmitted light, where the minimum cross-sectional area can be measured from the image taken because the minimum radius of a round bar specimen decreases after the maximum load point, while it remains almost circular [7, 23, 24].

However, the tensile specimens used in neutron irradiation tests are not miniature round bar specimens but miniature plate specimens for reasons of temperature control and temperature distribution during irradiation tests [25, 26]. Although there have been methods to experimentally determine the minimum cross-sectional area of plate specimens, such as attaching a mirror to the side of the specimen and obtaining dimensional deformation information on the side using digital image correlation technology [27, 28], the center of each face of a plate specimen is depressed and deformed, making it challenging to measure the cross-sectional area in the same way as for a round bar specimen. In addition, this method does not provide information in the depth direction, making it difficult to evaluate the minimum cross-sectional area in real time. The depth of focus of the optical system is critical to accurately measure the direction of depression, and a laser microscope is an imaging device with a deep depth of focus [29]. However, laser microscopes have the disadvantage that they take time to take a single image, and the tensile test must be interrupted each time the image is taken. Recently, with the development of shape measurement technology using laser profilers, there is now the possibility of measuring the minimum cross-sectional area of miniature plate specimens in real time using a high-speed laser profiler [30].

In this study, our focus is on the methodology of acquiring true stress-true strain from iFEM analysis and experimental methods for miniature plate specimens. The results of the iFEM analysis method were compared with those of miniature plate and round bar specimens. To introduce a novel experimental approach, we employed a high-speed laser profiler to measure the cross-sectional area and radius of curvature of necking in real time. We determined the true stresses and true strains using the acquired data and Bridgman's equation, and subsequently discussed the effectiveness of each method.

2. Experimental procedure

2.1. Material

In this study, the candidate material for fusion reactor structural materials is the reduced activation ferritic steel F82H. This material was developed around 1980 by Japan Atomic Energy Research Institute and NKK as an alternative to Mod.9Cr-1Mo steel, with improved creep strength and lower activation through the conversion of Mo to W and Nb to V in the (9-12) Cr-(1-2) Mo-VNb steel [31]. The specific material used in this study was F82H-BA07 (ID: 25A1-1), and its heat treatment conditions and chemical composition are presented in table 1. The material was produced using vacuum-induced melting followed by electroslag melting [32].

2.2. Inverse FEM

In recent years, an inverse analysis technique combined with the finite element method has been developed to obtain true stress-true strain curves for large strain regions, including materials after tension and expansion necking [16]. This method, known as the iFEM, is primarily used to obtain the true stress-true strain curve of the specimen in the finite element model using predefined true stress-true strain curves. The predefined true stress-true strain curve is then corrected by iteratively comparing finite element results with experimental results. The analysis flowchart of iFEM is provided in figures 1 and 2, and the specific steps are outlined as follows [17]:

Table 1. Chemical composition (mass%) and heat treatment condition of F82H-BA07.

C	Si	Mn	P	S	Cr	W	V	Ta	B	Cu	Ni
0.091	0.17	0.46	0.009	0.002	8.02	1.99	0.19	0.03	0.002	0.01	<0.01
Ti	Mo	Nb	Al	Co	Ag	Sn	As	Sb	O	N	Fe
<0.003	<0.01	<0.005	0.007	<0.01	<0.001	<0.003	<0.003	<0.003	0.001	0.016	Bal.

Heat treatment: normalizing:1040 °C × 40 min/AC + 960 °C × 30 min/AC; tempering: 750 °C × 60 min/AC.

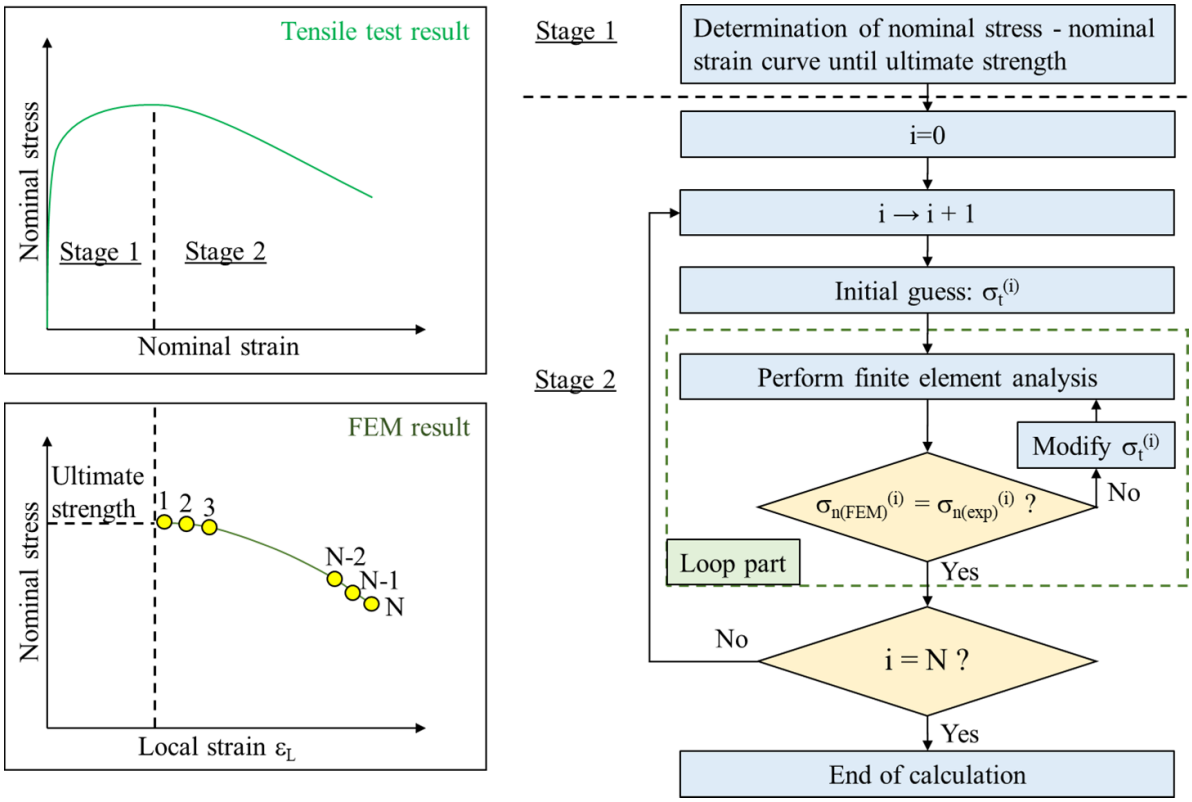

Figure 1. The analysis flowchart for determining the true stress-true strain curve [17].

- Firstly, the nominal stress-nominal strain curve of the material test specimen is obtained by conducting a tensile test until the necking strain is reached. The stress–strain curve is then divided into two stages: stage 1 from the beginning of stretching until the necking of the test specimen, and stage 2 from the beginning of necking of the test specimen until the end of stretching.
- For stage 1 before necking of the test specimen, the true stress-true strain curve of the corresponding part are obtained from the nominal stress-nominal strain curve of the experiment, using equations (1) and (2):

$$\sigma_t = \sigma_0 (1 + \varepsilon_0) \tag{1}$$

$$\varepsilon_t = \ln (1 + \varepsilon_0) \tag{2}$$

where σ_t: true stress, σ_0: nominal stress, ε_0: nominal strain, ε_t: true strain.

- For stage 2 after necking of the test specimen, the following four steps are followed to obtain the true stress-true strain curve:

  * Step 1: the sample point is determined by selecting the sample points from the nominal stress-nominal strain curve after necking.
  * Step 2: a segmented true stress-true strain curve is generated from the nominal stress-nominal strain curve obtained in Step 1. An arbitrary value of the true strain is specified for the first step, and the true stress-true strain curve is used to simulate the tensile test by finite element analysis (FEA).
  * Step 3: the true stress is determined by an iterative process. When the local strain at the center (neck) of the specimen reaches the corresponding local strain in the experimental data, the nominal stress is obtained by FEA. Local strain is defined here as the strain equivalent to the nominal strain at 5 mm gauge length of the specimen. Then, the true stress is changed to reduce the difference between the nominal stress obtained by FEA and the experimental nominal stress. The FEA is performed again using the changed true stress-true strain curve. This process is repeated until the nominal stress obtained by FEA matches the experimental nominal stress.

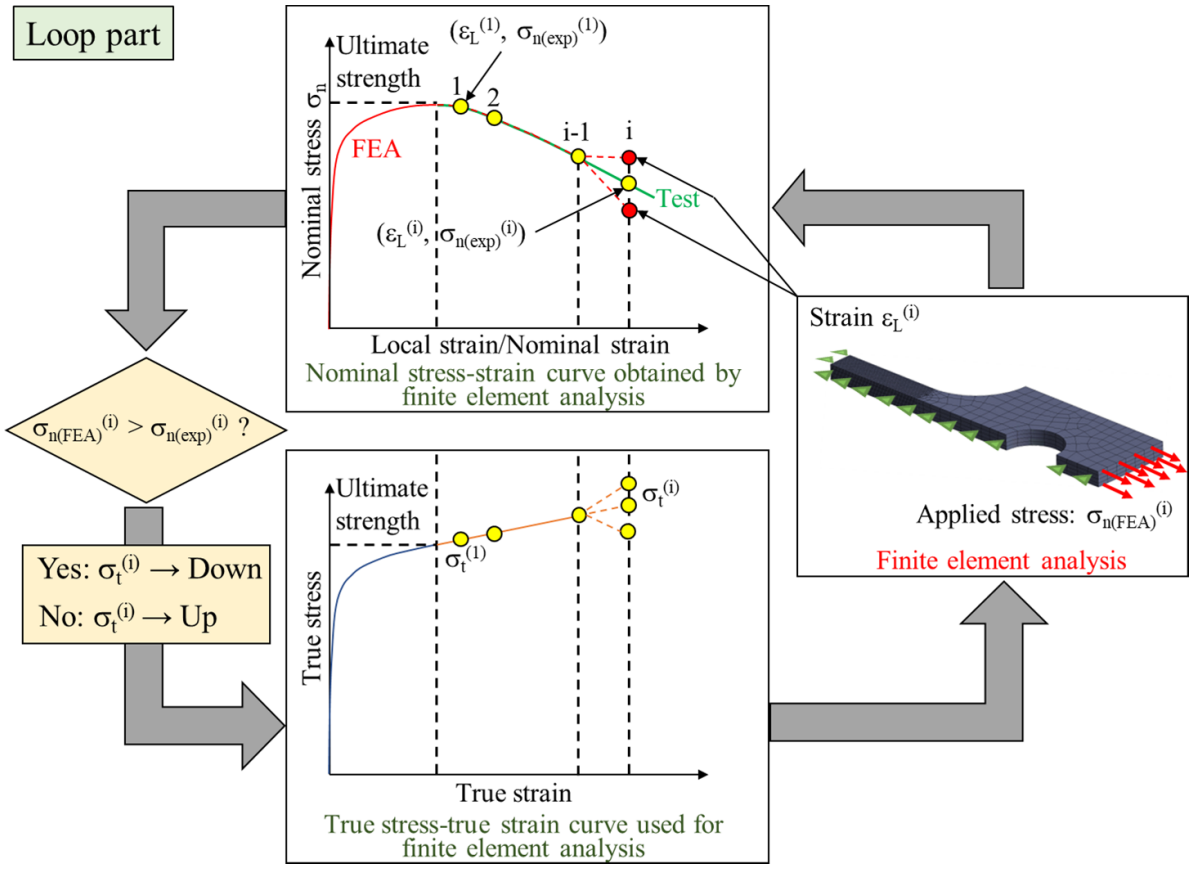

Figure 2. Detailed flowchart of loop part for determining true stress corresponding to the local strain measured by experiment [17].

* Step 4: the above process is repeated for the next sample point until all sample points are covered. The series of points (local strain, true stress) obtained in this way corresponds to the true stress-true strain curve after the necking strain. The predetermined true stress-true strain curve is considered the true stress-true strain curve of the analyzed material at the post-necking strain stage when the finite element results obtained by iterative iterations match the experimental results.

- Finally, the results of stage 1 and stage 2 are combined to obtain the complete true stress-true strain curve of the material. For more details on the iFEM analysis, please refer to papers [16, 17].

Previous research has demonstrated the applicability of the iFEM method to alloy steel materials, such as carbon steel and ferritic steel, with favorable outcomes [16, 18]. In this study, the true stress-true strain curves of F82H were analyzed using the iFEM and the commercial finite element software Ansys Workbench 2021R1 [33], following the steps outlined above.

A 3D model of the miniature plate specimen of F82H material is shown in figure 3(a), with dimensions consistent with those of the actual specimen. To reduce computational effort, a 1/8 model was used due to its symmetry. Figure 3(b) illustrates the boundary conditions of the analytical model. Symmetry boundaries are employed for the symmetry surfaces in the *x*, *y*, and *z* directions, with the *y*-directional symmetry symbols omitted. The *x*-directional tension is applied to the end face to simulate the tensile test. The local strain measurement area was refined in the model meshing to obtain accurate tensile strain results, with a cell size of 0.03 mm. The final 1/8 mesh model comprises 36 934 nodes and 7420 cells.

An elastoplastic analysis was employed to conduct the FEA of the tensile test. For metallic materials like F82H, a multilinear isotropic plastic hardening model was applied, which considers both large deformations and geometric nonlinear deformations. Young's modulus and Poisson's ratio were incorporated into the data at room temperature [34]. The iFEM analysis described above was used to obtain the true stress-true strain curve of the F82H material.

2.3. Tensile test, image measurement and high-speed profiler measurement

The specimen shape used in this study was the SS-J3 type (ID: SS-J3-A, B, C; gauge section: 1.2 w × 0.75 t × 5 l), which belongs to the category of miniature plate specimens, along with the miniature round bar type (ID: RB1, gauge section: ϕ1 × 5 l). The tensile test equipment used in this study was the Shimadzu Corp. AG-X 10 kN Plus, and the controller for image measurement was the Keyence Corp. XG-X2900. The

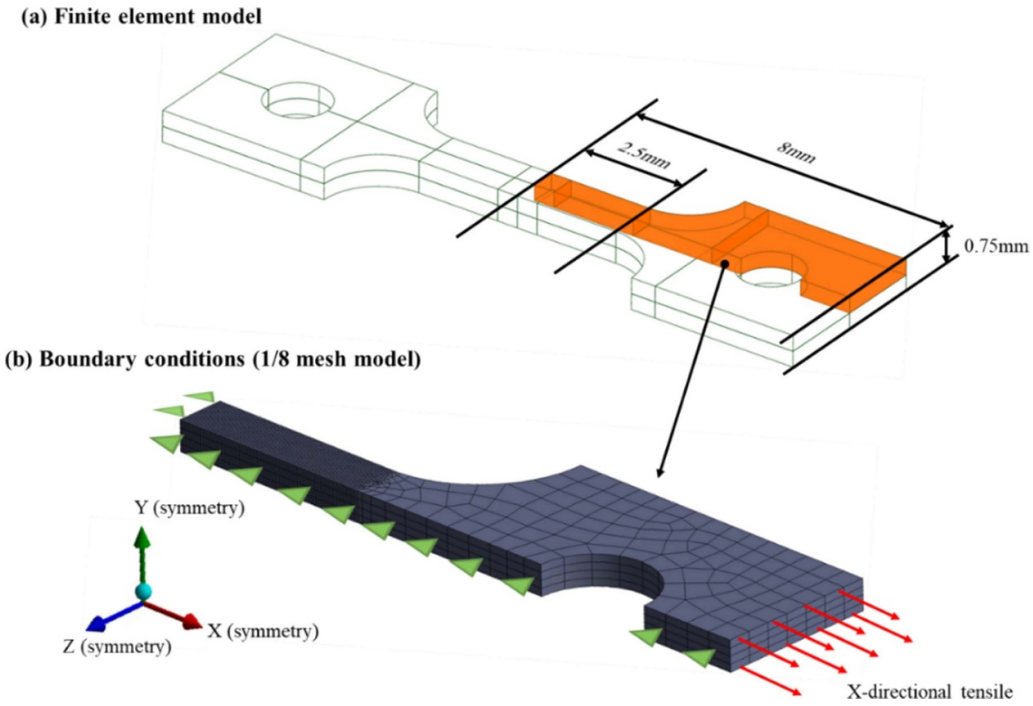

Figure 3. (a) Finite element model and (b) boundary conditions for miniature plate specimen.

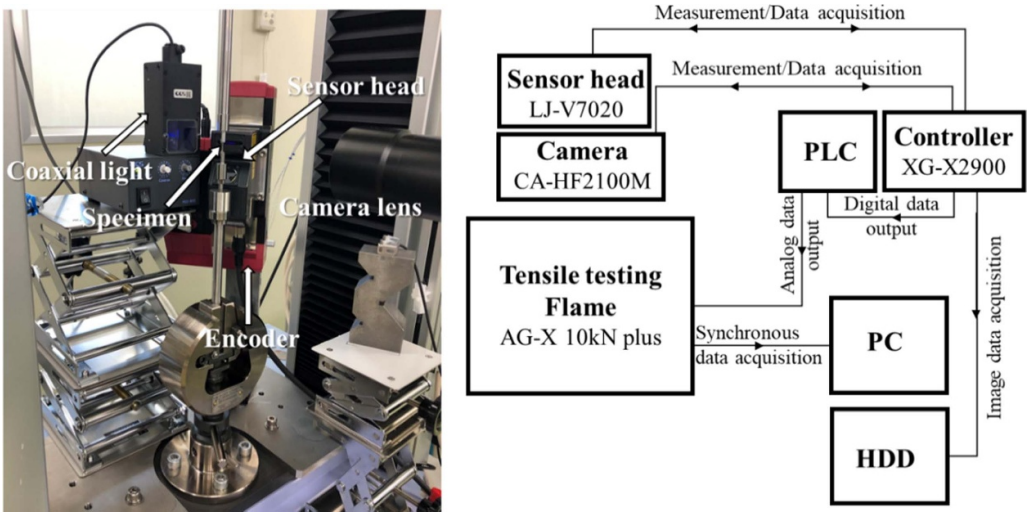

Figure 4. Tensile testing system including image measurement and laser profiler equipment.

camera used was the Keyence Corp. CA-HF2100M with 21 megapixels, and the lens was the VS Technology Corp telecentric lens VS-TCM07-150/S. The controller for the high-speed laser profiler was also the Keyence Corp. XG-X2900, which was used in conjunction with the image measurement system. The sensor head used was the Keyence Corp. LJ-V7020 with a focal length of 20 mm, and the light source for the image measurement was a transmitted light manufactured by CCS Inc. The configuration of the test system is shown in figure 4.

The high-speed laser profiler was operated reciprocally with the head section mounted on the IAI Corp. EC-S6SR-50 encoder and adjusted to a travel range of 10 mm and a speed of 20 mm s^{-1}. Tensile tests were conducted at a crosshead displacement rate of 0.03 mm min^{-1} (equivalent to a strain rate of 10^{-4} s^{-1}), a test temperature of room temperature, and a data sampling rate of 1 Hz. The LJ-V7020 was used to irradiate the laser beam onto the specimen to measure the minimum cross-sectional area and the radius of curvature at the neck. The measured data were analogically input to the tensile test equipment via the XG-X2900 and a programmable logic controller (PLC) link to synchronize the data with the tensile test results.

The laser head was set up to take images from an oblique direction to the specimen surface, as shown in figure 5. The cross-sectional area information obtained was for two

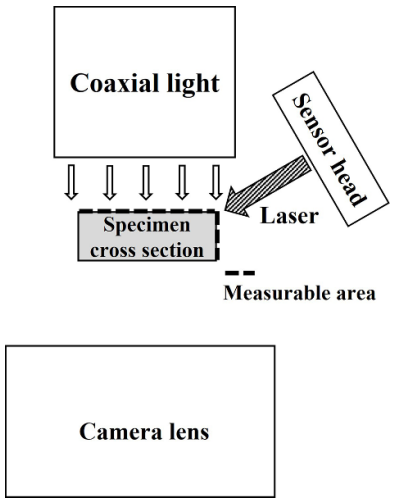

Figure 5. Schematic diagram of cross-sectional area measurement using by laser profiler and image.

surfaces, but the minimum cross-sectional area was calculated assuming that the other half, which could not be obtained, was equivalent to the measured cross-sectional area. The cross-sectional area was determined by subtracting the amount of change from the initial cross-sectional area. In the test program, the position where the radius of curvature contacts the specimen (axial distance from the bottom of the neck) needed to be set, and the measurement was performed by first setting the radius of curvature to meet the specimen at $X_0 = \pm 0.5$ mm, referring to values of $X_0 = 0.5$–0.6 mm reported in past papers [35].

2.4. True stress and true strain calculation

To calculate the true stress and true strain from the experimental data, equations (1) and (2) were applied, assuming that the volume remains constant during deformation up to the maximum load point.

Alternatively, the following equations can be used to calculate the true stress and true strain after the maximum load value has been reached in tensile tests using round bar specimens,

$$\sigma_{\mathrm{t}} = \frac{\sigma_{\mathrm{ave}}}{\left(1+\frac{2R}{r}\right)\ln\left(1+\frac{r}{2R}\right)} \tag{3}$$

$$\sigma_{\mathrm{ave}} = \frac{P}{A} \tag{4}$$

$$\varepsilon_{\mathrm{t}} = \ln\left(\frac{A_0}{A}\right) \tag{5}$$

where σ_{ave}: average stress, R: radius of curvature of local shrinkage, r: minimum radius of local shrinkage, P: incremental test load, A: incremental minimum cross-sectional area, A_0: initial cross-sectional area.

The following equations are utilized to compute the true stress and true strain after the maximum load value has been attained in tensile tests employing plate specimens,

$$\sigma_{\mathrm{t}} = \frac{\sigma_{\mathrm{ave}}}{\left(1+\frac{2R}{a}\right)^{0.5}\ln\left\{1+\frac{a}{R}+\left(\frac{2a}{R}\right)^{0.5}\left(1+\frac{a}{2R}\right)^{0.5}\right\}-1} \tag{6}$$

where a: incremental half-plate specimen width.

Bridgman's equations [15], represented by equations (3) and (6), are utilized for calculating the true stress after the maximum load value in tensile tests. As the specimen necks beyond the maximum load point, the stress state becomes multiaxial, but it is considered uniaxial for analysis purposes. Hence, the average stress obtained by dividing the test load at each moment by the minimum cross-sectional area, the radius of curvature at the neck, the minimum radius at the neck, and the half-width of the specimen are used to calculate the true stress. To use equations (3)–(6), it is necessary to measure the minimum cross-sectional area at each moment during the test.

3. Results

Figure 6 exhibits the experimental nominal stress-nominal strain curve obtained from the miniature plate specimen (SS-J3-A), along with the true stress-true strain curve obtained by iFEM analysis. It also shows the experimental nominal stress-nominal strain curve obtained from the miniature round bar specimen (RB1), and the true stress-true strain curves obtained from iFEM analysis. The graph reveals that there is no significant difference between the SS-J3-A and the RB1 specimens in both experimental and iFEM analysis results. They are in good agreement with each other, indicating that the iFEM analysis used in previous studies is a valid method for the materials and specimen sizes used in this study.

Furthermore, the results obtained from the combination of the image measurement device and the high-speed profiler are explained. Figure 7 illustrates the camera image (a), the contour diagram (b), and the cross-sectional profile (c) during the measurement. The arrowed area in the contour plot indicates the minimum cross-sectional area that has been measured. Since the measurement was taken from an oblique direction on the face of the specimen, the cross-sectional shape appears as half of the original cross-sectional shape.

Figure 8 shows a cross-sectional view of an interrupted specimen, which was stopped halfway through the tensile test and measured by a high-speed laser profiler, as well as observed under a stereo microscope. Although some differences exist in details such as edges, there is no difference between the cross-sectional area shape obtained by the laser profiler and the actual shape as a rough shape. The cross-sectional area of the interrupted specimen was 0.337 mm^2 when measured with a stereomicroscope after polishing the minimum cross-sectional area of the local shrinkage area. The cross-sectional area of the interrupted specimen obtained from the laser profiler was 0.342 mm^2. The difference between the cross-sectional area of the interrupted specimen and that obtained by the laser profiler was 0.005 mm^2 or 1.5%. This finding suggests that the cross-sectional area measured by the laser profiler is generally reasonable.

Figure 9 shows the nominal stress-nominal strain curve of SS-J3-B, along with the minimum cross-sectional area and

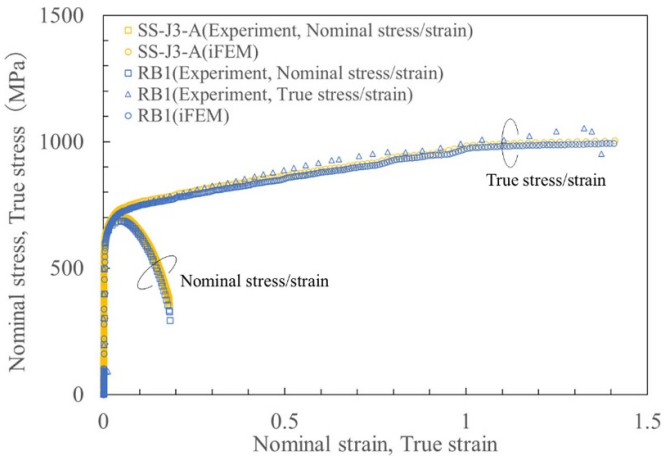

Figure 6. Nominal stress-nominal strain and true stress-true strain curve by experimental and iFEM.

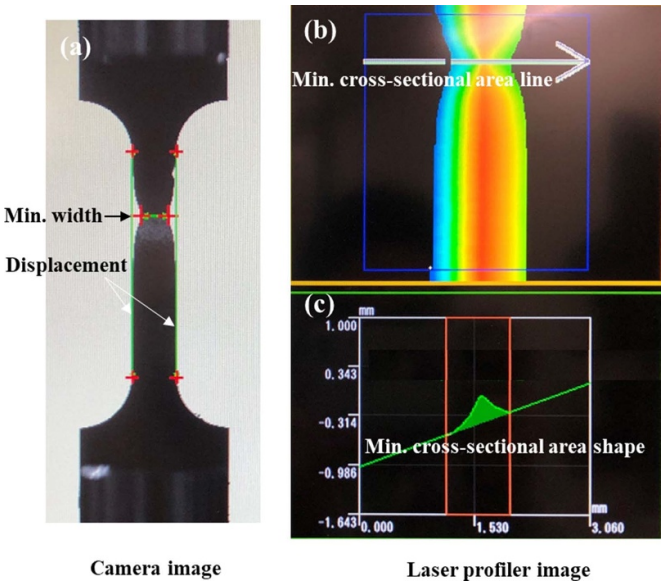

Figure 7. (a) Measurement of elongation of minimum specimen width by camera image, (b) contour diagram and (c) shape of half-size cross-sectional area. The arrow in (b) indicates the location of the minimum cross-sectional area.

radius of curvature plotted against strain. Additionally, the nominal stress-nominal strain curve of SS-J3-A obtained from the miniature plate specimen in figure 6 is also plotted. SS-J3-B was selected for comparison because the tensile strengths of SS-J3-A and SS-J3-B were relatively close, at 703 MPa and 697 MPa, respectively, at least in the stress–strain curves. As shown in figure 9(a), the fracture strain of SS-J3-B is 0.018 (1.8%) greater than that of SS-J3-A. The difference is believed to be due to the method used to measure elongation. Specifically, the elongation of SS-J3-A is measured and analyzed by the amount of deformation in the binarized specimen image obtained by coaxial light from behind the specimen. On the other hand, the elongation of SS-J3-B is measured and analyzed by the same method as SS-J3-A, but in addition to the elongation measurement, cross-sectional area and radius of curvature are also measured simultaneously. The laser beam overlaps with the point for measuring specimen elongation, resulting in partial halation of the image, which makes the image unrecognizable in the system. This factor is believed to lead to an overestimation of elongation (strain).

As explained above, the minimum cross-sectional area was determined as twice the cross-sectional area obtained by the high-speed laser profiler. It is observed that the minimum cross-sectional area decreases gradually until the tensile strength exceeds the maximum value, after which it drops sharply. This abrupt decline occurs at almost the same strain as the point where the tensile strength is reached, which is considered the critical point where uniform elongation ends and localized unstable deformation begins. The measurement accuracy of the radius of curvature was observed to change before and after the slope of the minimum cross-sectional area changed. This may be attributed to the detection sensitivity of the device, which was unable to detect the radius of curvature before necking became apparent near the minimum cross-sectional area, resulting in some dispersion. However, as necking became apparent, the detection sensitivity of the radius of curvature increased, and the measurement accuracy improved. Therefore, while there may be room for improvement in the measurement of elongation, the minimum cross-sectional area and the high-speed laser profiler were able to measure the minimum cross-sectional area and radius of curvature required for the calculation of true stress and true strain.

4. Discussion

To investigate the effect of variation in strain direction on the true stress-true strain curves, we compared the true stress-true strain curves obtained from experimental and iFEM analyses of SS-J3-A, SS-J3-B, and RB1. It should be noted that for SS-J3-A, only the results of the iFEM analysis were used as there is no information available on the radius of curvature and plate width measurements required for Bridgman's equation. Figure 10(a) presents a graph that plots each of these results together. While there are differences in the true strain at break, the iFEM analysis true stress-true strain curve for SS-J3-A, the experimental true stress-true strain curve for SS-J3-B, and the experimental and iFEM analysis true stress-true strain curves for RB1 generally agree. Figure 10(b) shows the difference (%) of true stress at each true strain for each specimen based on the iFEM results for SS-J3-A. Except for the iFEM results for SS-J3-B, the differences are within $\pm 5\%$ at each plot. Conversely, the iFEM results for SS-J3-B show that the difference increases as the true strain increases for true strains above 1.0. This finding suggests that inputting overestimated nominal stress-nominal strain curves into the iFEM analysis may result in a difference. Therefore, the nominal stress–nominal strain input into the iFEM analysis must be based on more precisely measured nominal stress-nominal strain data.

Equation (6) used to calculate the true stress comprises the following parameters: average stress (load and cross-sectional area), specimen half-width, and radius of curvature. Firstly, the effect of the radius of curvature was examined. Under the

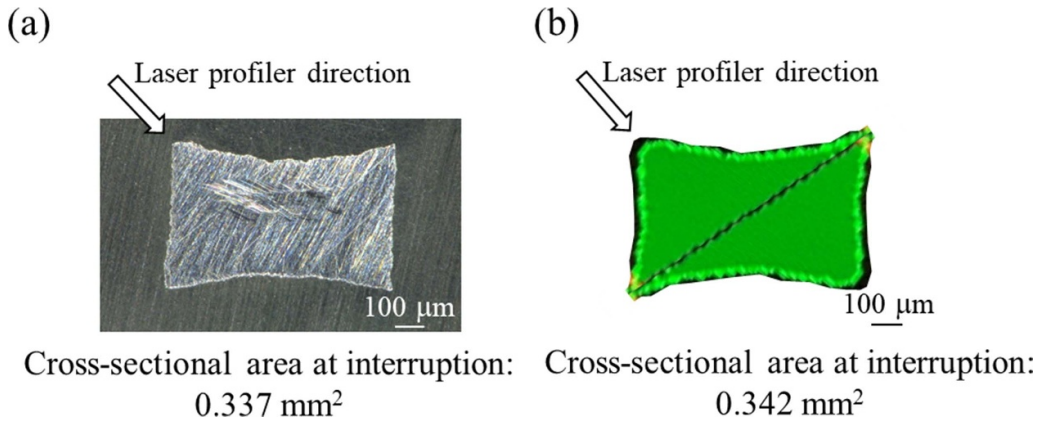

Figure 8. Comparison of cross-sectional shape acquired by (a) stereoscopic microscope and (b) laser profiler equipment of miniature plate specimen.

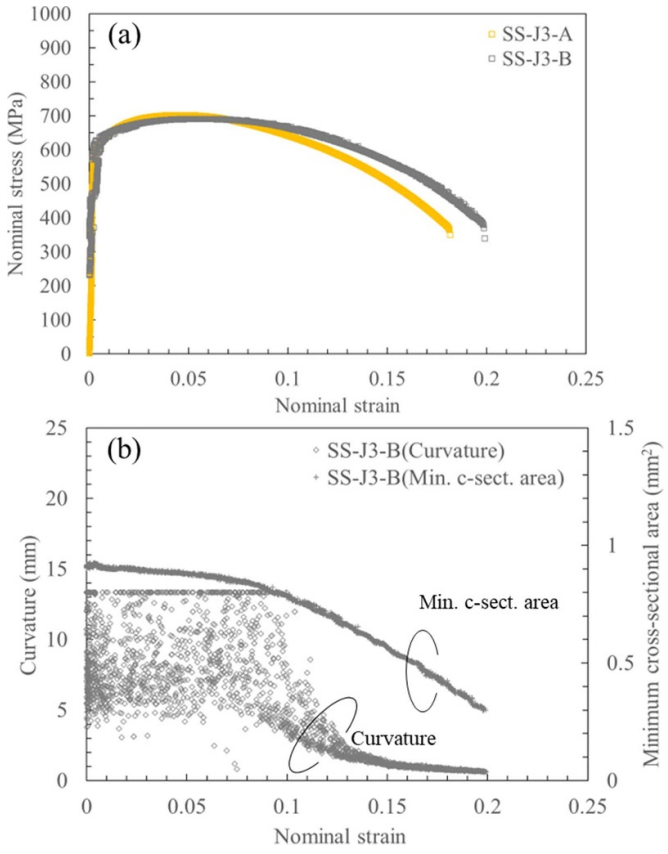

Figure 9. (a) Nominal stress-nominal strain curve, (b) Curvature and minimum cross-sectional area vs strain.

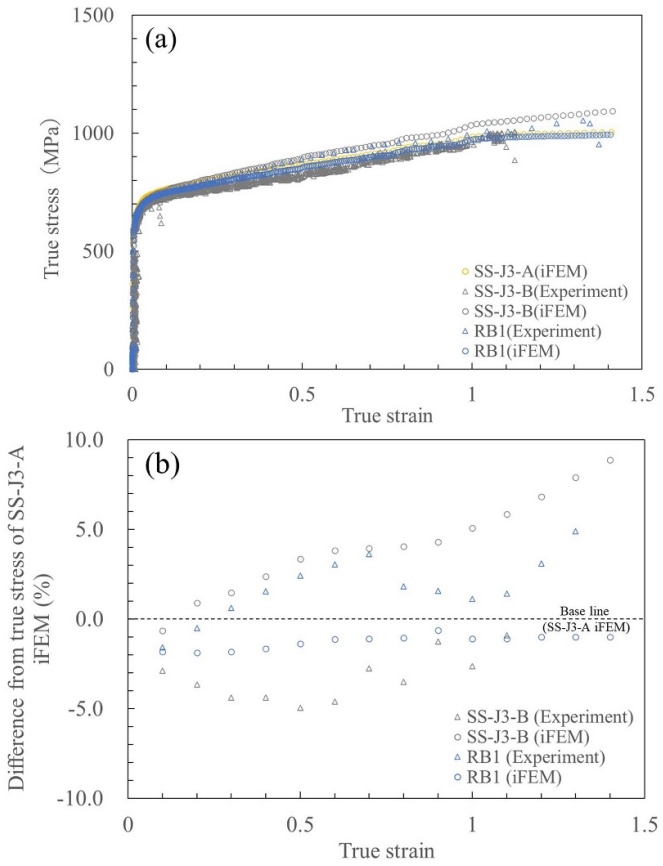

Figure 10. (a) Comparison of true stress of miniature plate specimen, miniature round specimen and iFEM and (b) Difference from the true stress of RB1 experiment for each specimen.

conditions of this study, where $X_0 = 0.5$ is set at the point where the radius of curvature contacts the specimen, there is a difference of about 10 MPa between the iFEM analysis results for RB1 and SS-J3-A and the results for SS-J3-B near the fracture strain ($\varepsilon_t = 1.1$). Since the value of the radius of curvature may also change by altering the value of X_0, we varied X_0 from 0.1 to 1.0 mm in 0.1 mm increments to investigate. The geometric relationship in the vicinity of the neck is shown in figure 11, with the origin at the bottom of the neck, the X-axis along the longitudinal direction of the specimen, and the Y-axis along the width direction [35]. The radius of curvature can be obtained by calculating the coordinates X_0 on the neckline as the distance between the observation points and Y_0 as the difference between the cross-sectional specimen half-width at the bottom of the neckline and the cross-sectional half-width of the adjacent observation points, using the relational equations shown in figure 11.

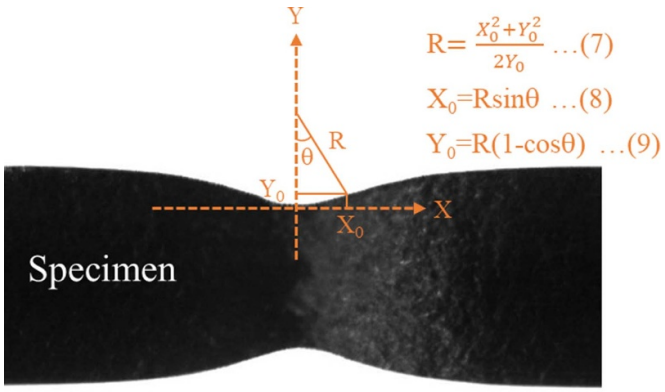

Figure 11. Geometric relationship near the neck and relationship equation [35].

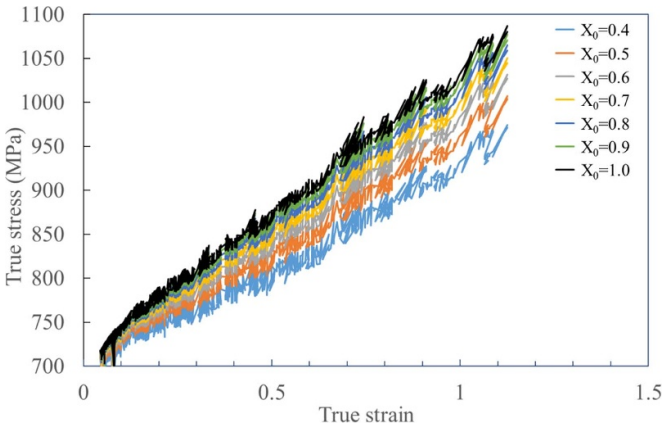

Figure 12. Results of the approximate equation for true stress using a radius of curvature obtained from the study.

The results of the study, which involved graphing the true stress using the radius of curvature obtained from the experiments, are presented in figure 12. When the radius of curvature was calculated with X_0 values ranging from 0.1 to 0.3, a decrease in true stress was observed near the true strain of 0.15 (close to the tensile strength). Consequently, the radius of curvature values obtained with $X_0 = 0.1$–0.3 was deemed unsuitable and was excluded from subsequent analysis. Figure 12 shows that the difference in true stress at each X_0 value increased as the true strain increased, and the maximum difference of true stress at $\varepsilon_t = 1.1$ was 108 MPa. The true stress at fracture obtained from iFEM analysis of RB1 and SS-J3-A at $\varepsilon_t = 1.1$ was 993 MPa and 983 MPa, respectively. By using these values as references, the difference between the true stress obtained from verification and the true stress obtained from iFEM of RB1 and SS-J3-A was determined. Table 2 shows the results. The smallest difference from the reference value was observed when X_0 was 0.5 mm, and this result indicates that the optimal X_0 value in this test is 0.5 mm, which is consistent with previous findings [35].

To confirm the influence of the radius of curvature on the calculation of true stress, a test was conducted with $X_0 = 0.7$ mm. The true stress-true strain curves obtained from

Table 2. Difference between the true stress calculated by iFEM analysis for RB1 and SS-J3-A at each X_0 of $\varepsilon_t = 1.1$.

X_0 (mm)		0.4	0.5	0.6	0.7	0.8	0.9	1.0
RB1	MPa	18	14	38	56	70	81	91
	%	1.8	1.4	3.8	5.6	7.1	8.2	9.2
SS-J3-A	MPa	28	4	28	46	60	71	81
	%	2.8	0.4	2.8	4.6	6.0	7.1	8.1

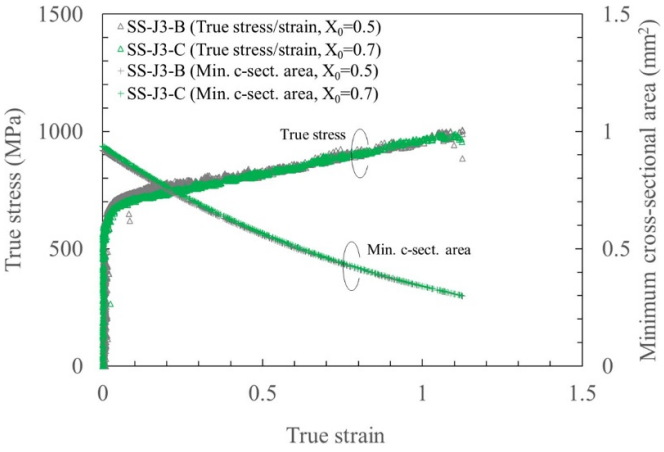

Figure 13. Comparison of true stress and minimum cross-sectional area of SS-J3-B ($X_0 = 0.5$) and SS-J3-C ($X_0 = 0.7$).

measurements at $X_0 = 0.5$ mm (SS-J3-B) and $X_0 = 0.7$ mm (SS-J3-C) are shown in figure 13. While it would have been ideal to replace $X_0 = 0.5$ with $X_0 = 0.7$ in the measurement of SS-J3-B and reanalyze the results, this was not possible. Therefore, SS-J3-C ($X_0 = 0.7$) was selected for comparison as it has a relatively similar stress–strain curve to that of SS-J3-B and does not have $X_0 = 0.5$. As shown in the graph, there is a slight difference in some portions, but there is almost no difference at 14 MPa near the fracture position. These results suggest that the value of the radius of curvature has minimal effect on the calculated true stress results with the degree of variation observed in this study.

Subsequently, the effect of the minimum cross-sectional area was examined, as depicted in figure 13. The results show no significant variation in either case. Furthermore, as stated in the results section, the measurements obtained from the high-speed profiler are not significantly different from the true values. Therefore, the minimum cross-sectional area values measured in this study are not expected to significantly impact the calculated true stress results.

Finally, the specimen width was examined. The specimen width obtained in this study was measured from the projected image and was taken at the outermost side in the thickness direction. However, the smallest specimen width, which is concave compared to the surface side of the thickness, is located at the center of the thickness direction, as shown in figure 8. The true stress-true strain curve recalculated using the minimum width at the center, calculated using the ratio of the width measured by projection from the cross-sectional image

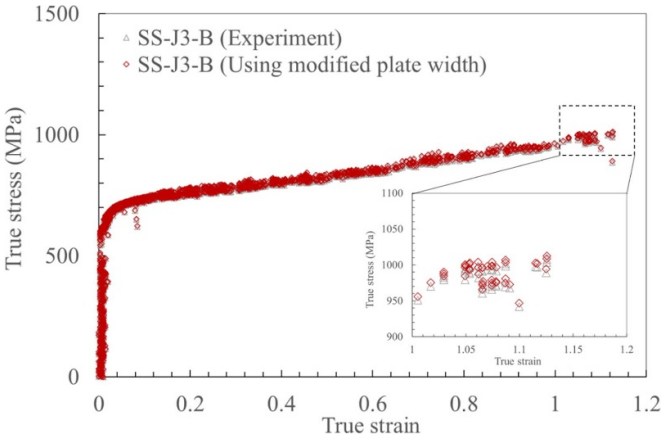

Figure 14. Comparison of true stresses for different plate widths.

to the minimum width at the center, is shown in figure 14 along with the true stress-true strain curve calculated using the specimen width in the projection image. It can be seen that the true stress calculated using the minimum plate width is higher than the true stress calculated using the width measured from the projection image, although the increase is negligible at 5 MPa in this test. For specimens that are more concave in the center of the thickness, the increase in true stress is expected to be more pronounced compared to the true stress calculated using the plate width on the surface side of the thickness. Therefore, to calculate the true stress more accurately, it is important to use the specimen plate width value at the point where the specimen plate width near the center of the specimen thickness is the minimum value. However, since the difference is not extremely large, it may be possible to simply calculate the true stress using the measurement results of the outermost specimen width.

5. Summary

In this study, our focus was on two methods to obtain the true stress-true strain relationship using iFEM analysis and experimental methods for miniature plate specimens. We compared the iFEM analysis results with the true stresses obtained from experimental methods for miniature plate and round bar specimens, as well as with iFEM analysis results for those specimens. The difference in true stress was within ±5% compared to the true stresses obtained from the experimental methods for both miniature plate and round bar specimens. However, an overestimation of the true stress can result from inputting overestimated nominal strain into the iFEM results.

We introduced a new laser profiler that enables real-time measurement of the cross-sectional area and radius of curvature of the necking of a miniature plate specimen. Using the measured data and the separately measured specimen width, the true stress obtained from Bridgman's equation was found to be accurate to within 5%, as demonstrated above.

These results indicate that analytical methods utilizing iFEM analysis and experimental methods utilizing a laser profiler are effective in determining the true stress-true strain of miniature plate specimens.

Data availability statement

All data that support the findings of this study are included within the article (and any supplementary files).

ORCID iD

Taichiro Kato https://orcid.org/0000-0002-6581-9776

References

[1] Imura H 2004 Japanese policy on the science and technology research *J. Nucl. Mater.* **329–333** 1–4
[2] Kohyama A 2005 Current status of fusion reactor structural materials R&D *Mater. Trans.* **46** 384–93
[3] Hirose T, Okubo N, Tanigawa H, Ando M, Sokolov M A, Stoller R E and Odette G R 2011 Irradiation hardening in F82H irradiated at 573 K in the HFIR *J. Nucl. Mater.* **417** 108–11
[4] Miwa Y, Wakai E, Shiba K, Hashimoto N, Robertson J P, Rowcliffe A F and Hishinuma A 2000 Swelling of F82H irradiated at 673K up to 51 dpa in HFIR *J. Nucl. Mater.* **283–287** 334–8
[5] Wakai E, Hishinuma N, Miwa Y, Robertson J P, Klueh R L, Shiba K and Jitsukawa S 2000 Effect of helium production on swelling of F82H irradiated in HFIR *J. Nucl. Mater.* **283–287** 799–805
[6] Kohno Y, Gelles D S, Kohyama A, Tamura M and Hishinuma A 1992 Irradiation response of a reduced activation Fe-8Cr-2W martensitic steel (F82H) after FFTF irradiation *J. Nucl. Mater.* **191–194** 868–73
[7] Nozawa T, Sakasegawa H, Chen X, Kato T, Geringer J W, Katoh Y and Tanigawa H 2020 Non-contact strain evaluation for miniature tensile specimens of neutron-irradiated F82H by digital image correlation *Fusion Eng. Des.* **157** 111663
[8] Oka H, Hashimoto N, Muroga T, Kimura A, Sokolov M A, Yamamoto T and Ohnuki S 2014 Hardness distribution and tensile properties in an electron beam weldment of F82H irradiated in HFIR *J. Nucl. Mater.* **455** 454–9
[9] Taguchi T, Jitsukawa S, Sato M, Matsukawa S, Wakai E and Shiba K 2004 Post irradiation plastic properties of F82H derived from the instrumented tensile tests *J. Nucl. Mater.* **335** 457–61
[10] Ando M, Tanigawa H, Kurotaki H and Katoh Y 2018 Mechanical properties of neutron irradiated F82H using micro-tensile testing *Nucl. Mater. Energy* **16** 258–62
[11] Tanigawa H, Diegele E, Katoh Y, Nozawa T, Hirose T, Gorley M, Sakasegawa H, Gaganidze E, Aktaa J and Pintsuk G 2018 The strategy of fusion DEMO in-vessel structural material development *27th IAEA Fusion Energy Conf., Proc.* IAEA-CN-258/ OV3-4
[12] Tanigawa H 2018 Technical challenges on material and design criteria development for fusion in-vessel components *Fusion Eng. Des.* **133** 89–94
[13] MacGregor C W 1944 The true stress-strain tension test—its role in modern materials testing: part I *J. Frankl. Inst.* **238** 111–35
[14] MacGregor C W 1944 The true stress-strain tension test—its role in modern materials testing: part II *J. Frankl. Inst.* **238** 159–76

[15] Bridgman P W 1952 *Studies in Large Plastic Flow and Fracture* (New York: McGraw-Hill) pp 9–37
[16] Kamaya M and Kawakubo M 2011 A procedure for determining the true stress—strain curve over a large range of strains using digital image correlation and finite element analysis *Mech. Mater.* **43** 243–53
[17] Kamaya M, Kitsunai Y and Koshiishi M 2015 True stress-strain curve acquisition for irradiated stainless steel including the range exceeding necking strain *J. Nucl. Mater.* **465** 316–25
[18] Maloy S A, Saleh T A, Anderoglu O, Romero T J, Odette G R, Yamamoto T, Li S, Cole J I and Fielding R 2016 Characterization and comparative analysis of the tensile properties of five tempered martensitic steels and an oxide dispersion strengthened ferritic alloy irradiated at ∼295 °C to ∼6.5 dpa *J. Nucl. Mater.* **468** 232–9
[19] Yazzile K E, Williams J J and Chawla N 2012 Quantifying necking of rectangular tensile specimens using a mirror-based image analysis system *Mater. Lett.* **74** 243–6
[20] Chen B and Pan B 2022 Measuring true stress-strain curves of cylindrical bar samples with mirror-assisted multi-view digital image correlation *Strain* **58** e12403
[21] Careglio C A, Celentanl D J, García Garino C G and Mirasso A E 2016 Global and local mechanical responses for necking of rectangular bars using updated and total Lagrangian finite element formulations *Math. Probl. Eng.* **2016** 1729638
[22] Cabezas E E and Celentano D J 2004 Experimental and numerical analysis of the tensile test using sheet specimens *Finite Elem. Anal. Des.* **40** 555–75
[23] Sakasegawa H, Chen X, Kato T, Tanigawa H, Ando M, Geringer J W, Ukai S and Ohtsuka S 2018 Strain evaluation using a non-contact deformation measurement system in tensile tests of irradiated F82H and 9Cr ODS steels *Nucl. Mater. Energy* **16** 108–13
[24] Kato T, Ohata M, Nogami S and Tanigawa H 2016 Evaluation of impacts of stress triaxiality on plastic deformability of RAFM steel using various types of tensile specimen *Fusion Eng. Des.* **109–111** 1631–6
[25] Qualls A L and Muroga T 1998 A varying temperature irradiation experiment for operation in HFIR *J. Nucl. Mater.* **258–263** 407–12
[26] Longest A W, Corum J E, Heatherly D W and Thoms K R 1988 Design of spectrally tailored fusion reactor materials experiments in the HFIR RB capsule irradiation facility *J. Nucl. Mater.* **155–157** 1346–9
[27] Li J, Yang G, Siebert T, Shi M F and Yang L 2018 A method of the direct measurement of the true stress-strain curve over a large strain range using multi-camera digital image correlation *Opt. Lasers Eng.* **107** 194–201
[28] Milosevic N, Younise B, Sedmak A, Travica M and Mitrovic A 2021 Evaluation of true stress-strain diagrams for welded joints by application of digital image correlation *Eng. Fail. Anal.* **128** 105609
[29] Minsky M 1961 Microscopy apparatus *US Patent* 3013467
[30] Keyence Corporation of America High-speed 2D/3D laser profiler (available at: www.keyence.com/products/measure/laser-2d/lj-v/) (Accessed 21 December 2022)
[31] Tamura M, Hayakawa H, Tanimura M, Hishinuma A and Kondo T 1986 Development of potential low activation ferritic and austenitic steels *J. Nucl. Mater.* **141–143** 1067–73
[32] Tanigawa H, Shiba K, Sakasegawa H, Hirose T and Jitsukawa S 2011 Technical issues related to the development of reduced -activation ferritic/martensitic steels as structural materials for a fusion blanket system *Fusion Eng. Des.* **86** 2549–52
[33] ANSYS 2021 *PDF Documentation for Release 2021R2* (Canonsburg, PA: ANSYS Inc)
[34] Nozawa T *et al* 2021 The status of the Japanese material properties handbook and the challenge to facilitate structural design criteria for DEMO in-vessel components *Nucl. Fusion* **61** 116054
[35] Murayama N, Torizuka S, Hanamura T and Imagumbai M 2012 Tensile test method with image analysis to obtain true stress-true strain curve up to fracture *Tetsu-to-Hagane* **98** 415–24 (in Japanese)